ROYAL SOCIETY
OF CHEMISTRY

PAPER

Check for updates

Photothermal synthesis of a CuO$_x$&FeO$_y$ catalyst with a layered double hydroxide-derived pore-confined frame to achieve photothermal CO$_2$ hydrogenation to CO with a rate of 136 mmol min^{-1} g$_{cat}$$^{-1}$†

Lizhu Song,[a] Xinli Yi,[a] Shuxin Ouyang [ID] *[b] and Jinhua Ye [ID] [ac]

Solar-driven CO$_2$ conversion into the industrial chemical CO *via* the reverse water–gas reaction is an ideal technological approach to achieve the key step of carbon neutralization. The high reaction temperature is cost-free due to the photothermal conversion brought about by solar irradiation and is beneficial to the catalytic efficiency. However, the thermostability of adopted catalysts is a great challenge. Herein, we develop an *in situ* photothermal synthesis to obtain a CuO$_x$&FeO$_y$ catalyst with a layered double hydroxide-derived pore-confined frame. The optimized sample delivers a CO generation rate of 136.3 mmol min^{-1} g$_{cat}$$^{-1}$ with the selectivity of ~100% at a high reaction temperature of 1015 °C. The efficient catalytic activity can be attributed to the fact that the pore-confined frame substrate prevents the growth of CuO$_x$ and FeO$_y$ nanoparticles during the high-temperature reaction and the basic groups on the substrate promote the adsorption and activation of CO$_2$.

Introduction

Carbon dioxide (CO$_2$), a typical greenhouse gas, has a significant impact on the climate of the earth, and carbon neutralization consumes huge amounts of energy due to the inertness of CO$_2$.[1] Nowadays, profiting from photothermocatalysis driven by sunlight, the catalytic conversion of CO$_2$ into various value-added chemicals (alkanes, alcohols, and other multi-carbon organics) *via* the photothermal reverse water–gas shift (RWGS) reaction (CO$_2$ + H$_2$ ↔ CO + H$_2$O)[2,3] followed by Fischer–Tropsch synthesis (FTS: nCO + 2nH$_2$ → C$_n$H$_{2n}$ + nH$_2$O)[4] is a feasible and almost energy cost-free "two-step" approach for carbon recycling.[2,5] However, the high yield rate and near-unity selectivity of CO during the photothermal RWGS reaction step is still a challenge so that the ratio of the feedstock gases (syngas, CO and H$_2$) for the subsequent Fischer–Tropsch synthesis can be facilely tuned and rapidly imported.[6]

Cu-based catalysts stand out among the various high CO-selective catalysts because of their abundant resources and

[a]TJU-NIMS International Collaboration Laboratory, School of Materials Science and Engineering, Tianjin University, Tianjin 300072, P. R. China

[b]Key Laboratory of Pesticide and Chemical Biology, Ministry of Education, College of Chemistry, Central China Normal University, Wuhan 430079, P. R. China. E-mail: oysx@mail.ccnu.edu.cn

[c]International Center for Materials Nanoarchitectonics (WPI-MANA), National Institute for Materials Science (NIMS), 1-1 Namiki, Tsukuba 305-0047, Japan

† Electronic supplementary information (ESI) available. See https://doi.org/10.1039/d2na00315e

low price.[7] As summarized in Table 1, the CO selectivity of Cu-based catalyst is close to 100%.[8–11] Hydrocarbons such as CH$_4$ are nearly impossible to form,[7,12] even under H$_2$-rich conditions (H$_2$ > 99 vol%).[13] The RWGS reaction is mildly endothermic ($\Delta H^{\ominus}_{298}$ = 42.1 kJ mol^{-1}),[3] and a higher reaction temperature is beneficial for promoting the catalytic efficiency.[14] However, Cu-based catalysts exhibit poor thermostability, which makes them prone to sintering aggregation during the high-temperature RWGS reaction, since the Tammann temperature of Cu films is low (~930 K, satisfying the general trend that the Tammann temperature is normally about 2/3 of a material's melting temperature).[15] In addition, photothermal catalysts with other metal elements as active components, such as 2D Black In$_2$O$_{3-x}$,[16] C–In$_2$O$_{3-x}$,[17] Co@CoN&C,[18] and Fe@C,[19] are still suitable for low-temperature photothermal catalysis.[20] Therefore, achieving the thermostability of adopted catalysts for the high-temperature photothermal RWGS reaction is a great challenge.

The widely adopted modifications to enhance the thermostability of catalysts, such as adding precious metals[21–24] or constructing core/shell structures,[25,26] are expensive or/and involve complex synthesis, which are difficult to apply in industry. Herein, we demonstrate an *in situ* photothermal synthesis to obtain a CuO$_x$&FeO$_y$ catalyst with a layered double hydroxide-derived pore-confined frame, which prevents the growth of CuO$_x$ and FeO$_y$ nanoparticles during the high-temperature reaction, and the basic groups on the catalyst promote the adsorption and activation of CO$_2$. Under focused

Table 1 Activities over representative catalytic systems for the RWGS reaction

| Catalyst	Preparation	Reaction tem. (°C)	CO rate (mmol min^{-1} g$_{cat}^{-1}$)	CO$_2$ con. (%)	CO sel. (%)	Ref.
Thermal catalysis						
10%Cu5%Fe/CeO$_2$	900–1000 °C 400 °C, 4 h	650	0.4	42	100	8
0.3CuMgAl-LDH	500 °C, ∼	350	0.2	32.9	99.8	9
CuO/ZnO/Al$_2$O$_3$	400 °C, 8 h	250		17		10
Cu–Fe/SiO$_2$	600 °C, 5 h	600		15		11
Photothermal catalysis						
2D Black In$_2$O$_{3-x}$	150 °C, 2 h	340	1.7	53.3	100	16
C–In$_2$O$_{3-x}$	600 °C, 4 h	400	2.1	45	100	17
Co@CoN&C	550 °C, 4 h	518	2.2	41.3	91.1	18
Fe@C	500 °C, 2 h	481	0.4		99.7	19
CuO$_x$&FeO$_y$/MAO	700 °C, 2 h ∼^{a}	1015 (P.T.)^b	136.3	45.6	100	This study

^{a} The synthesis of the catalyst did not undergo any thermal reduction process. ^{b} P.T.: photothermal.

sunlight irradiation simulated by a Xe lamp, the RWGS reaction can proceed over the CuO$_x$&FeO$_y$/MAO catalyst at a high temperature of 1015 °C to deliver a stable CO yield rate of 136.3 mmol min^{-1} g$_{cat}^{-1}$ and a near 100% selectivity for 10 hours. The apparent activity of CuO$_x$&FeO$_y$/MAO remarkably surpasses that of the representative catalysts in thermocatalysis or photothermocatalysis, as listed in Table 1.

Results and discussion

The pre-catalyst was prepared *via* an impregnation method with Cu(NO$_3$)$_2$·3H$_2$O, Fe(NO$_3$)$_3$·9H$_2$O and commercial Mg$_6$-Al$_2$(CO$_3$)(OH)$_{16}$·4H$_2$O (Mg,Al-LDH) as raw materials. Then, the pre-catalyst was photothermally treated in a flow-type reactor (Fig. S1, ESI†) under the RWGS reaction atmosphere to obtain the final catalyst (denoted as CuO$_x$&FeO$_y$/MAO). The proposed formation mechanism of the Mg,Al-LDH derivative-confined CuO$_x$&FeO$_y$ catalyst is presented in Scheme 1. Under a rising

temperature *via* light-to-heat conversion and an atmosphere of CO$_2$ and H$_2$, the loaded Cu^{2+} and Fe^{3+} in the impregnation process (Scheme 1a) were reduced to Cu and Fe NPs, respectively (Scheme 1b). Due to the generation of H$_2$O, the surface of the nano-metals was partially oxidized to their respective oxides (Cu$_2$O and Fe$_3$O$_4$). The localized photothermal effect of the nano-metals led to a phase transformation of the hydroxide into amorphous phase oxides (MgO and Al$_2$O$_3$, MAO), causing a thermal etching effect and forming a porous structure at the surface (inset of Scheme 1b), which can be evidenced by the measurements of the BET surface area and pore-structure analysis (Table S1† and Fig. 1a). These surface pores confine the growth of CuO$_x$ and FeO$_y$. Due to the different growth rates, some ultrafine FeO$_y$ NPs locate around CuO$_x$ (Scheme 1c), which stabilizes the size and chemical valence of CuO$_x$ (which will be discussed in a later section in detail). The high-melting-point materials of MgO and Al$_2$O$_3$ construct a high-temperature-stable substrate, which plays an
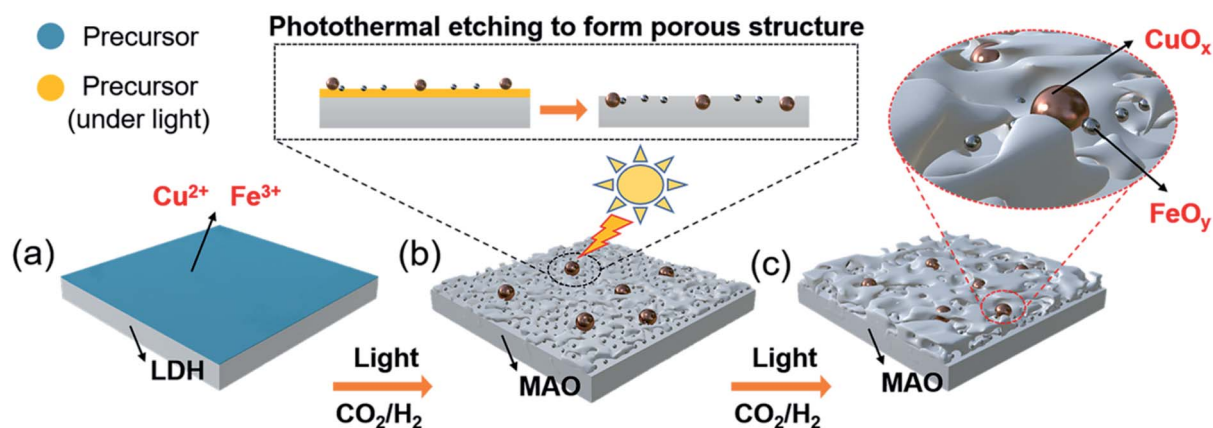
Scheme 1 Proposed synthetic mechanism of the Mg,Al-LDH-derived MAO frame-confined CuO$_x$&FeO$_y$ catalyst. (a) Catalyst precursor prepared by impregnation process; (b) photothermal etching process at the initial reaction stage; (c) Schematic microstructure of the CuO$_x$&FeO$_y$/MAO after reaction.
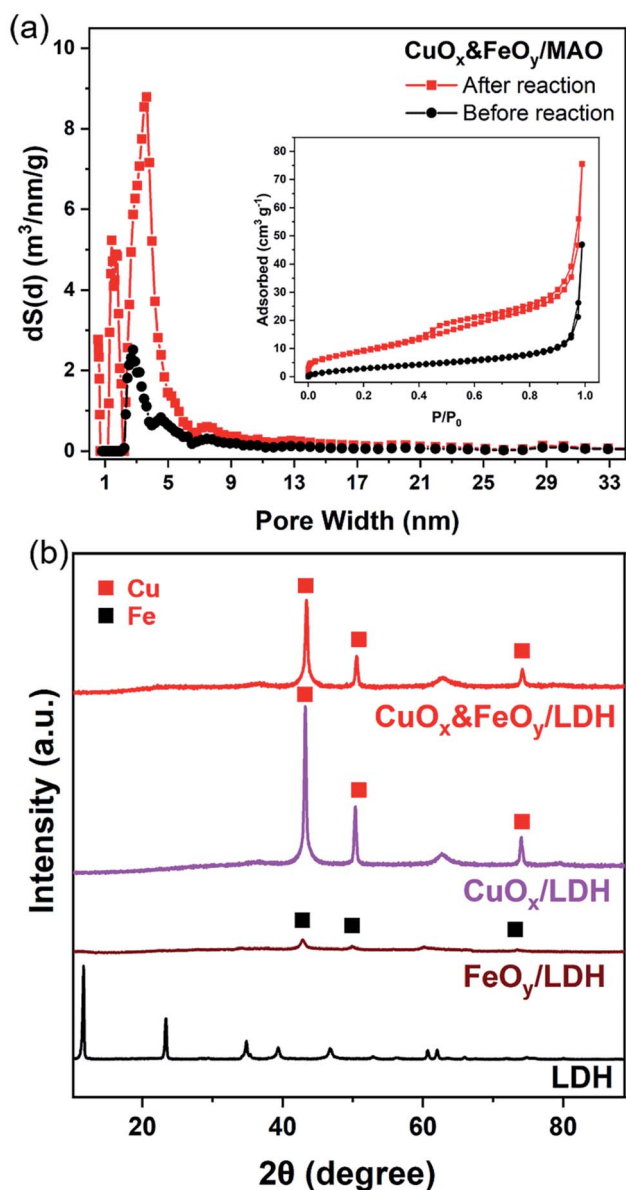
© 2022 The Author(s). Published by the Royal Society of Chemistry

Fig. 1 (a) Nitrogen adsorption−desorption isotherms of the CuO$_x$&FeO$_y$/MAO precursor and sample after reaction (inset: pore-size distribution curves). (b) XRD patterns of LDH, CuO$_x$/MAO and CuO$_x$&FeO$_y$/MAO.

important role in reinforcing the stability of the newly formed porous structure.

X-ray diffraction (XRD) and X-ray photoelectron spectroscopy (XPS) were adopted to determine the phase compositions and the chemical valence of the elements in the samples before and after the reaction. After the photothermocatalytic RWGS reaction, the XRD patterns of CuO$_x$&FeO$_y$/MAO (Fig. 1b) mainly present the characteristic peaks of metallic Cu, while the two peaks near 38° and 62° cannot be assigned to a specific phase. According to the XPS results (Fig. 2), the peaks at the binding energies of 932.5, 934.6 and 941.8 eV are related to the Cu and Cu$_2$O, CuO, and satellite peaks, respectively.[12,27] Three peaks were observed at 709.4, 710.4, and 711.6 eV, which can be
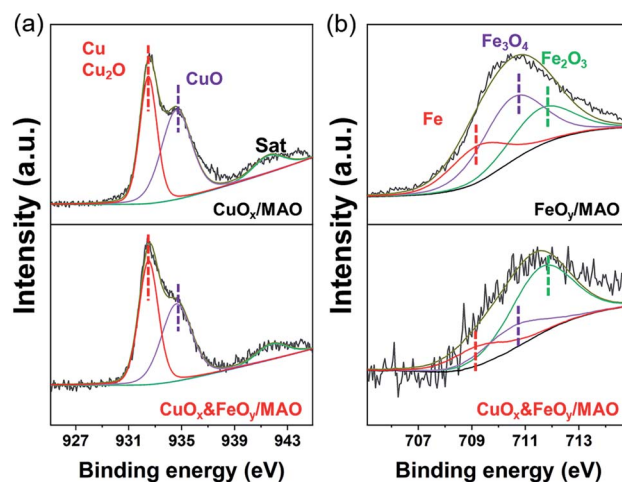

Fig. 2 XPS spectra of CuO$_x$&FeO$_y$/MAO, CuO$_x$/MAO and FeO$_y$/MAO: (a) Cu 2p; (b) Fe 2p.

assigned to metallic Fe, Fe$_3$O$_4$, and Fe$_2$O$_3$, respectively. Therefore, the Cu- and Fe-related compositions in the catalyst are designated as CuO$_x$ and FeO$_y$, respectively. The possible phase compositions related to the Mg and Al elements are partially crystallized or amorphous MgO and Al$_2$O$_3$, as previously reported,[28] and therefore, the substrate is denoted as MAO.

As shown in Fig. S2 (ESI†), the commercial Mg,Al-LDH features a smooth and flat sheet morphology. However, the SEM image of CuO$_x$&FeO$_y$/MAO after a 10 h photothermal RWGS reaction (Fig. 3a) indicates a complex pore structure on the surface of the catalyst substrate. In the TEM and high-resolution TEM (HRTEM) images (Fig. 3b, d and e), the dark sphere-like particles can be identified as metallic Cu according to the 0.21 nm lattice fringes associated with the Cu(111) crystal plane; therefore, a certain number of these Cu nanoparticles (NPs) were selected to survey their size and their average diameter is 22.9 nm (inset of Fig. 3b). Moreover, the pore structures on the substrate surface can be clearly observed due to the shallow contrast, and their sizes mainly distribute around 5 nm (Fig. 3e). Elemental mapping of CuO$_x$&FeO$_y$/MAO (Fig. 3c) revealed that the Cu element distribution is highly concentrated, which is well consistent with the bright spots of the HAADF-TEM image. The Fe element presents a relatively aggregated distribution around Cu, and thus, the XRD patterns exhibit that the Cu composition is crystallized, while the featured peaks of Fe cannot be observed. Based on the calculation of the overlapping colorful regions in the elemental mapping of Cu and Fe, it can be estimated that about 40.9% of the Fe NPs are in close contact with Cu NPs. The Mg, Al, and O elements are uniformly dispersed, suggesting that they are the main components of the substrate. These results are well consistent with the characterization results of XRD. Thus, the above characterizations reveal the formation of the well-dispersed active phase on the porous-structured substrate. The Fe-free catalyst SEM and TEM images demonstrate the significant agglomeration of metallic Cu NPs, as can be seen in Fig. S3 (ESI†).
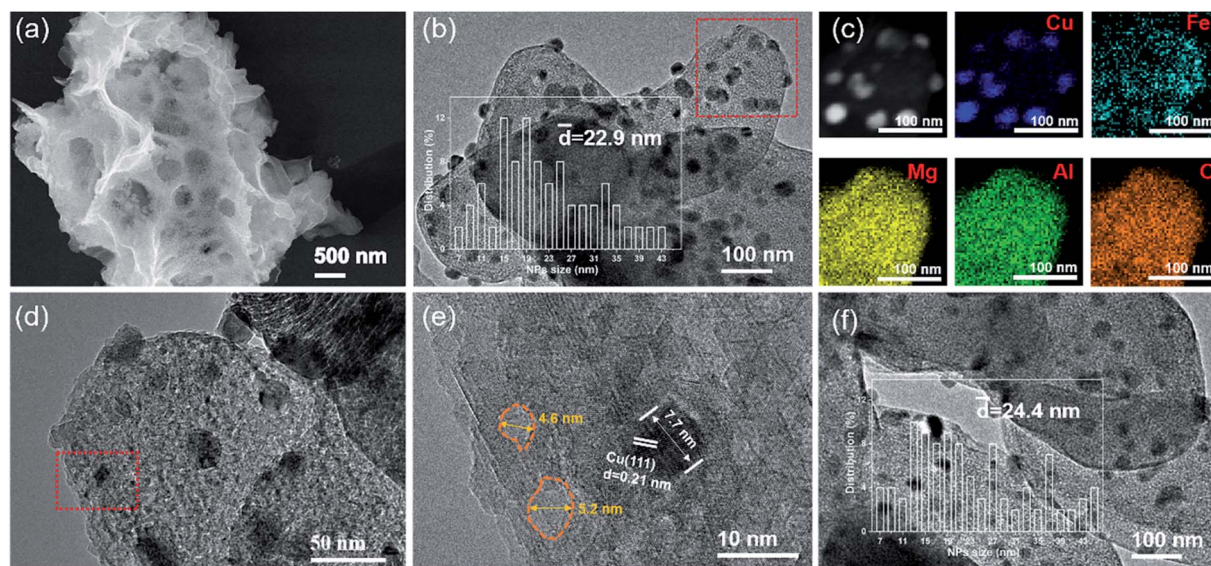
Fig. 3 Microstructure of CuO_x&FeO_y/MAO. (a) SEM image; (b) TEM image and Cu NP size distribution (10 h); (c) HAADF–TEM image and mapping of Cu, Fe, Mg, Al and O; (d) and (e) HRTEM; (f) TEM image and Cu NP size distribution (40 h).

Photothermal catalysts require a wide wavelength region of light absorption to attain efficient light-to-heat conversion. The UV-visible absorption spectra of the catalysts after the RWGS reaction are shown in Fig. S4 (ESI†). It can be observed that CuO_x&FeO_y/MAO and the two reference catalysts of CuO_x&FeO_y/MgO and CuO_x&FeO_y/Al_2O_3 exhibit intense light absorption in the UV and visible regions. In general, the substrate affects the light absorption property of the catalyst, and the MAO substrate with pores strongly promotes the absorption intensity of the catalyst, which might be attributed to multi-light reflections by the porous surface. Accordingly, the light-to-heat conversion efficiency of CuO_x&FeO_y/MAO is higher than that of the other two catalysts. Its equilibrium temperature is as high as 1015 °C, which is 40 °C and 56 °C higher than that of the other two catalysts, respectively (Fig. S5, ESI†).

To verify that CuO_x&FeO_y/MAO can prevent sintering aggregation, the photothermal catalysis of the reverse water–gas shift (RWGS) reaction over the as-prepared catalysts was carried out in a flow-type reaction system at a working temperature higher than 950 °C. As presented in Fig. 4a, the average CO yield rate of CuO_x&FeO_y/MAO is 136.3 mmol min^{-1} g$_{cat}$$^{-1}$ with a selectivity of ~100% and an average CO_2 conversion of 41.3% during 10 h light irradiation. The various active phases (CuO_x or FeO_y) and substrates (MgO or Al_2O_3) were substituted in the mixture of CuO_x and FeO_y and MAO to explore their roles in enhancing the catalytic activity and stability (Fig. 4a). The key findings can be summarized as follows. First, while adopting the same substrate of MAO, the catalytic activity order is CuO_x&FeO_y/MAO > CuO_x/MAO > FeO_y/MAO and the activity of CuO_x&FeO_y/MAO (136.3 mmol min^{-1} g$_{cat}$$^{-1}$) is even higher than the sum (86.3 + 41.9 mmol min^{-1} g$_{cat}$$^{-1}$) of the activities of the two latter catalysts, indicating that the composite of CuO_x and FeO_y is a superior active phase. Second, the CO evolution rates over CuO_x&FeO_y/MAO and FeO_y/MAO exhibit good sustainability. In
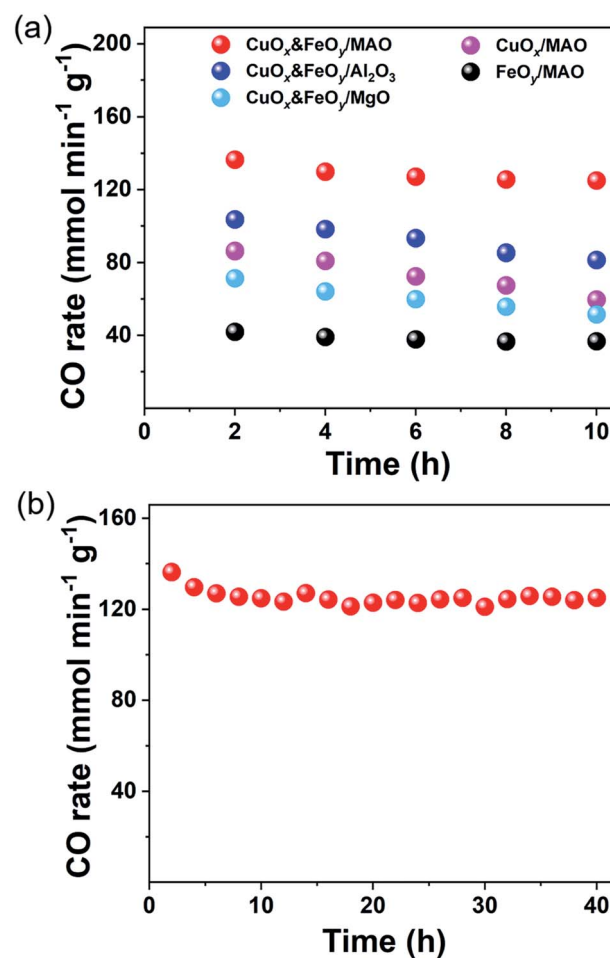

Fig. 4 Photothermal RWGS reaction tests. (a) CO yield rate. (b) Long-term stability testing over CuO_x&FeO_y/MAO.

comparison, the CO yield rates over $CuO_x\&FeO_y/Al_2O_3$, $CuO_x\&FeO_y/MgO$, CuO_x/MAO, and FeO_y/MAO have fallen by roughly 21.4%, 27.8%, 31.0%, and 12.1%, respectively, after the initial 10 h reaction. The Fe-free catalyst of CuO_x/MAO suffers from the most serious deactivation, indicating that FeO_y plays a role in promoting the activity stability.[29,30] To confirm the excellent stability of $CuO_x\&FeO_y/MAO$ at high reaction temperatures, a long-term stability test (40 h) was conducted (Fig. 4b). The average CO yield rate was 124.9 mmol min^{-1} g$_{cat}^{-1}$ during continuous 40 h testing; after the long-term stability test, the average size of the Cu NPs is 24.4 nm (Fig. 3f), which is comparable to that before the reaction (22.9 nm), indicating that the confined frame of MAO and FeO_y indeed prevent the sintering aggregation of the Cu NPs. Compared with the stable $CuO_x\&FeO_y/MAO$ catalyst, SEM and TEM indicate obvious agglomeration of the catalysts with Al_2O_3 (Fig. S6, ESI†) or MgO (Fig. S7, ESI†) as substrates after the 10 h photothermal RWGS reaction, which may be the primary reason for the decrease in catalytic activity. The XRD patterns of the two samples are shown in Fig. S8, ESI.† Moreover, a contrast experiment was carried out to prove the necessity of the localized photothermal effect of the nano-metals to form the porous structure of the MAO substrate, which confined the growth of the nano-metals. The contrast sample was prepared by thermal reduction of the pre-catalyst powder in a tube furnace at 1015 °C for 2 h under a H_2/Ar (10 v%/90 v%) atmosphere and labeled as T-$CuO_x\&FeO_y$/MAO. The XRD patterns (Fig. S9, ESI†) indicate that the catalyst carrier was composed of $MgAl_2O_4$ and MgO. The specific surface area of T-$CuO_x\&FeO_y$/MAO (110.8 m^2 g^{-1}) exceeded three times that of $CuO_x\&FeO_y$/MAO after reaction (Fig. S10, ESI†). However, the CO production rate was 91.4 mmol min^{-1} g$_{cat}^{-1}$, in conjunction with a downward trend of activity in the first 2 hours (Fig. S11, ESI†). The SEM and TEM images of T-$CuO_x\&FeO_y$/MAO after the photothermal RWGS reaction show a significant agglomeration of metallic Cu NPs (Fig. S12, ESI†).

The Fourier transform infrared (FT-IR) spectra were recorded to explore the CO_2 conversion over the surface of the catalysts. The results were analyzed by referring to previous literature.[31] Compared with the fresh LDH carrier (Fig. S13, ESI†), the FT-IR spectra of the spent $CuO_x\&FeO_y$/MAO catalyst (Fig. S14, ESI†) indicate the conversion of absorbed CO_2 into the easily activated form of carbonate/bicarbonate (CO_3^{2-}/HCO_3^-). CO_3^{2-}/HCO_3^- was reduced to formate species by the dissociation of H on Cu NPs. CO_3^{2-}/HCO_3^- bands were observed at 880 cm^{-1} [IV] and 1448 cm^{-1} [II, $\nu(OCO)_s$]. The $CuO_x\&FeO_y$/MAO catalyst showed the strongest absorption band at 1448 cm^{-1}, indicating that it possesses an abundance of HCO_3^-, which is easier to convert into formate species than CO_3^{2-}. The high-temperature stabilization of bridge formate (br-HCOO) on the catalyst surface was detected at 1635 cm^{-1} [I, asymmetrical, $\nu(OCO)_{as}$] and 1384 cm^{-1} [III, symmetrical, $\nu(OCO)_s$]. The generated formate species further decomposed into CO and regenerated OH^-.[32]

The mechanism of the Mg,Al-LDH-derived MAO frame-confined $CuO_x\&FeO_y$ catalyst with efficient and stable catalytic performance under high temperature can be summarized as follows. Since Cu NPs are the active phase, the microstructure feature and the chemical environment around them affect the catalytic performance (Fig. 5). Fe-based materials are often applied as promoters to improve the thermal stability and catalytic activity of RWGS catalysts.[8,11,30,33–35] Firstly, the Fe-based promoter exhibits much better dispersity than the active phase of Cu (which can be evidenced by the TEM and elemental mapping results of $CuO_x\&FeO_y$/MAO, Fig. 3). The ultrafine and amorphous FeO_y NPs around the crystallized CuO_x also protect the CuO_x NPs from sintering growth, especially along the surface (Scheme 1b), which promotes the thermal stability significantly. Secondly, the introduction of Fe oxide increased the basic sites of the catalyst and enhanced the adsorption ability of CO_2 (Fig. S15, ESI†).[11] Moreover, as seen in the XPS results, the Cu 2p$^{3/2}$ binding energy in $CuO_x\&FeO_y$/MAO shifted negatively compared to that in CuO_x/MAO, suggesting that low-valence Cu was significantly more abundant in the former. This can be attributed to the fact that the Cu-FeO_y interfacial region provides more active sites for H_2 dissociation than individual Cu and Fe, and therefore transfers active H to Cu, which maintains the low chemical valence of Cu.[33,36] This can be supported by the fact that the introduction of excessive Fe results in the formation of CH_4 (Fig. S16, ESI†). The amorphous MAO substrate derived from Mg,Al-LDH possesses abundant surface basic groups, which facilitate the chemical adsorption, activation and conversion of CO_2; the relevant processes are shown as chemical equations in Fig. 5b.[37] The basic active sites over the $CuO_x\&FeO_y$/MAO catalyst feature

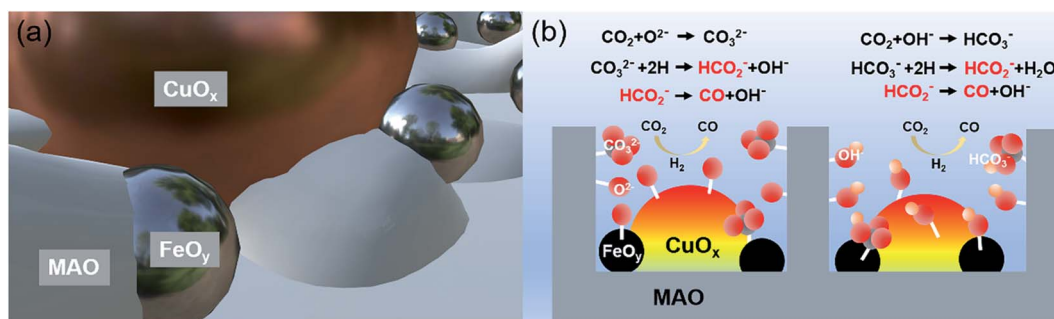**Fig. 5** Mechanism of the Mg,Al-LDH-derived MAO frame-confined $CuO_x\&FeO_y$ catalyst with efficient and stable catalytic performance under high temperatures. (a) Space confined effect. (b) Abundant basic groups.

cyclic regeneration, which can be evidenced by the FT-IR spectra after the photothermal reaction (Fig. S14, ESI†). Besides, according to our reported method,[12] contrast activity evaluations under light irradiation with or without UV light were carried out; the performance exhibits a slight reduction in the absence of UV light, indicating a coupling effect of photothermocatalysis and photocatalysis (Fig. S17, ESI†).

Conclusions

In summary, a CuO_x&FeO_y catalyst with an LDH-derived pore-confined frame was prepared by an *in situ* photothermal procedure in the RWGS reaction atmosphere. The introduction of an Fe-based promoter stabilized the low chemical valence of Cu in CuO_x, leading to excellent RWGS activity. The pore-confined frame consisted of Mg,Al-LDH in the bulk and a mixture of MgO and Al_2O_3 on the surface, which provided a thermally stable porous structure with abundant basic groups. Besides suppressing the growth of CuO_x and FeO_y NPs, this unique substrate promoted the adsorption and activation of CO_2. The above-mentioned advantages enable CuO_x&FeO_y/MAO to exhibit durable activity in the RWGS reaction at a photothermally induced high temperature of 1015 °C. The catalyst delivered a CO yield rate of 136.3 mmol min^{-1} g$_{cat}^{-1}$ with near-unity selectivity. Our study provides a facile and cost-efficient method to prepare high-temperature-capable catalysts, which extends the solar-driven photothermocatalysis application to the working temperature range of 1000 °C.

Experimental section

The experimental details are provided in the ESI.†

Author contributions

Lizhu Song and Shuxin Ouyang conceived the study. Lizhu Song and Xinli Yi performed the experiments and carried out the material characterization. Lizhu Song, Xinli Yi, Shuxin Ouyang and Jinhua Ye analyzed the results and wrote the manuscript. All authors participated in the discussion and interpretation of the results.

Conflicts of interest

There are no conflicts to declare.

Acknowledgements

Notes and references

1 Y. Xu, P. N. Duchesne, L. Wang, A. Tavasoli, A. A. Jelle, M. Xia, J. Liao, D. Kuang and G. A. Ozin, *Nat. Commun.*, 2020, **11**, 5149.

2 Y. Ma, Z. Guo, Q. Jiang, K. Wu, H. Gong and Y. Liu, *J. Energy Chem.*, 2020, **50**, 37–43.

3 Y. A. Daza and J. N. Kuhn, *RSC Adv.*, 2016, **6**, 49675–49691.

4 F. Jiao, J. Li, X. Pan, J. Xiao, H. Li, H. Ma, M. Wei, Y. Pan, Z. Zhou, M. Li, S. Miao, J. Li, Y. Zhu, D. Xiao, T. He, J. Yang, F. Qi, Q. Fu and X. Bao, *Science*, 2016, **351**, 1065–1068.

5 M. Wang, M. Shen, X. Jin, J. Tian, M. Li, Y. Zhou, L. Zhang, Y. Li and J. Shi, *ACS Catal.*, 2019, **9**, 4573–4581.

6 J. Li, Y. He, L. Tan, P. Zhang, X. Peng, A. Oruganti, G. Yang, H. Abe, Y. Wang and N. Tsubaki, *Nat. Catal.*, 2018, **1**, 787–793.

7 F. Liu, L. Song, S. Ouyang and H. Xu, *Catal. Sci. Technol.*, 2019, **9**, 2125–2131.

8 L. Chen, D. Wu, C. Wang, M. Ji and Z. Wu, *J. Environ. Chem. Eng.*, 2021, **9**, 105183.

9 Y. Chen, H. Hong, J. Cai and Z. Li, *ChemCatChem*, 2021, **13**, 656–663.

10 M. J. L. Ginés, A. J. Marchi and C. R. Apesteguía, *Appl. Catal., A*, 1997, **154**, 155–171.

11 M. González-Castaño, J. C. Navarro de Miguel, F. Sinha, S. Ghomsi Wabo, O. Klepel and H. Arellano-Garcia, *J. CO2 Util.*, 2021, **46**, 101493.

12 L. Zhao, Y. Qi, L. Song, S. Ning, S. Ouyang, H. Xu and J. Ye, *Angew. Chem., Int. Ed.*, 2019, **58**, 7708–7712.

13 Y. Tong, L. Song, S. Ning, S. Ouyang and J. Ye, *Appl. Catal., B*, 2021, **298**, 120551.

14 X. Su, X. Yang, B. Zhao and Y. Huang, *J. Energy Chem.*, 2017, **26**, 854–867.

15 G. Mahmud, H. Zhang and J. F. Douglas, *J. Chem. Phys.*, 2020, **153**, 124508.

16 Y. Qi, L. Song, S. Ouyang, X. Liang, S. Ning, Q. Zhang and J. Ye, *Adv. Mater.*, 2020, **32**, 1903915.

17 Y. Qi, J. Jiang, X. Liang, S. Ouyang, W. Mi, S. Ning, L. Zhao and J. Ye, *Adv. Funct. Mater.*, 2021, **31**, 2100908.

18 S. Ning, H. Xu, Y. Qi, L. Song, Q. Zhang, S. Ouyang and J. Ye, *ACS Catal.*, 2020, **10**, 4726–4736.

19 H. Zhang, T. Wang, J. Wang, H. Liu, T. D. Dao, M. Li, G. Liu, X. Meng, K. Chang, L. Shi, T. Nagao and J. Ye, *Adv. Mater.*, 2016, **28**, 3703–3710.

20 X. Zhu, J. Liu, X. Li, J. Liu, X. Qu and A. Zhu, *J. Energy Chem.*, 2017, **26**, 488–493.

21 K. Suzuki, T. Yamaguchi, K. Matsushita, C. Iitsuka, J. Miura, T. Akaogi and H. Ishida, *ACS Catal.*, 2013, **3**, 1845–1849.

22 G. Ren, Y. Tang, K. Liu, Y. Su, S. Miao, W. Liu, W. Cong, X. Wang, W. Li, J. Li and T. Zhang, *Nano Lett.*, 2018, **18**, 6489–6493.

23 B. Puértolas, Á. Mayoral, R. Arenal, B. Solsona, A. Moragues, S. Murcia-Mascaros, P. Amorós, A. B. Hungría, S. H. Taylor and T. García, *ACS Catal.*, 2015, **5**, 1078–1086.

24 C. Moreno, N. J. Divins, J. Gázquez, M. Varela, I. Angurell and J. Llorca, *Nanoscale*, 2012, **4**, 2278–2280.

25 R. Jin, J. Easa and C. P. O'Brien, *ACS Appl. Mater. Interfaces*, 2021, **13**, 38213–38220.

26 D. Lou, Z. Zhu, Y.-F. Xu, C. Li, K. Feng, D. Zhang, K. Lv, Z. Wu, C. Zhang, G. A. Ozin, L. He and X. Zhang, *Sci. China Mater.*, 2021, **64**, 2212–2220.

27 Z. Zhang, S.-S. Wang, R. Song, T. Cao, L. Luo, X. Chen, Y. Gao, J. Lu, W.-X. Li and W. Huang, *Nat. Commun.*, 2017, **8**, 488.

28 U. Sharma, B. Tyagi and R. V. Jasra, *Ind. Eng. Chem. Res.*, 2008, **47**, 9588–9595.

29 J. Liu, A. Zhang, X. Jiang, M. Liu, Y. Sun, C. Song and X. Guo, *ACS Sustainable Chem. Eng.*, 2018, **6**, 10182–10190.

30 C. Chen, W. Cheng and S. Lin, *Appl. Catal., A*, 2004, **257**, 97–106.

31 N. C. Nelson, M.-T. Nguyen, V.-A. Glezakou, R. Rousseau and J. Szanyi, *Nat. Catal.*, 2019, **2**, 916–924.

32 N. Ishito, K. Hara, K. Nakajima and A. Fukuoka, *J. Energy Chem.*, 2016, **25**, 306–310.

33 L. Yang, L. Pastor-Pérez, J. J. Villora-Pico, A. Sepúlveda-Escribano, F. Tian, M. Zhu, Y. Han and T. Ramirez Reina, *ACS Sustainable Chem. Eng.*, 2021, **9**, 12155–12166.

34 C. Chen, W. Cheng and S. Lin, *Chem. Commun.*, 2001, **18**, 1770–1771.

35 Q. Zhang, L. Pastor-Pérez, Q. Wang and T. Ramirez Reina, *J. Energy Chem.*, 2022, **66**, 635–646.

36 M. Zhu, P. Tian, M. E. Ford, J. Chen, J. Xu, Y.-F. Han and I. E. Wachs, *ACS Catal.*, 2020, **10**, 7857–7863.

37 J. Ren, S. Ouyang, H. Xu, X. Meng, T. Wang, D. Wang and J. Ye, *Adv. Energy Mater.*, 2017, **7**, 1601657.